

PARTICLE-IN-CELL SIMULATIONS OF PARTICLE ENERGIZATION VIA SHOCK DRIFT ACCELERATION FROM LOW MACH NUMBER QUASI-PERPENDICULAR SHOCKS IN SOLAR FLARES

JAEHONG PARK^{1,2}, CHUANG REN^{1,2,3}, JARED C. WORKMAN^{4,1}, AND ERIC G. BLACKMAN^{1,2}

¹Department of Physics & Astronomy, University of Rochester, Rochester NY, 14627

²Laboratory for Laser Energetics, University of Rochester, Rochester NY, 14623

³Department of Mechanical Engineering, University of Rochester, Rochester NY, 14627 and

⁴Department of Physical & Environmental Sciences, Colorado Mesa University, Grand Junction CO, 81501

Draft version September 3, 2018

ABSTRACT

Low Mach number, high beta fast mode shocks can occur in the magnetic reconnection outflows of solar flares. These shocks, which occur above flare loop tops, may provide the electron energization responsible for some of the observed hard X-rays and contemporaneous radio emission. Here we present new 2D particle-in-cell simulations of low Mach number/high beta quasi-perpendicular shocks. The simulations show that electrons above a certain energy threshold experience shock-drift-acceleration. The transition energy between the thermal and non-thermal spectrum and the spectral index from the simulations are consistent with some of the X-ray spectra from RHESSI in the energy regime of $E \lesssim 40 \sim 100$ keV. Plasma instabilities associated with the shock structure such as the modified-two-stream and the electron whistler instabilities are identified using numerical solutions of the kinetic dispersion relations. We also show that the results from PIC simulations with reduced ion/electron mass ratio can be scaled to those with the realistic mass ratio.

Subject headings: PIC simulation, solar flares, low Mach number shocks, shock drift acceleration, modified two-stream, whistler instabilities

1. INTRODUCTION

Low Mach number (M), high plasma beta (β_p) fast mode shocks can occur in the magnetic reconnection outflows of solar flares. Hard X-ray data from Yohkoh and RHESSI has revealed that electrons are energized above flare loop tops and foot points (e.g., Lin et al. 2003). Solar flares are diverse and the associated reconnection events are likely “acceleration environments” with potentially different mechanisms of particle acceleration operating on different scales. One potential source of particle acceleration, seen from analytic predictions (Blackman & Field 1994) and numerical simulations of reconnection configurations in which an obstacle was present (e.g., Forbes 1998; Workman et al. 2011), involves the presence of low Mach number fast shocks in reconnection outflows. These “termination” shocks may contribute to the high energy acceleration observed over some frequency range, studying the potential ways in which these shocks can accelerate particles is well motivated.

Mann et al. (2006, 2009) and Warmuth et al. (2009) suggested an electron energization via shock drift acceleration (hereafter SDA) in termination shocks. Guo & Giacalone (2010, 2012) performed hybrid simulations for termination shocks where test electrons were effectively energized via the interaction with pre-existing large-scale magnetic fluctuations. In our recent work (Park et al. 2012), we performed a full particle-in-cell (PIC) simulation for purely perpendicular (i.e. magnetic field perpendicular to the shock normal), low M /high β_p shocks. We found that both electrons and ions participated in SDA.

Termination shocks may however deviate from purely perpendicularity in solar flares, the extent to which is an open question. In the meantime, it is instructive to relax

the constraint that the shocks are exactly perpendicular and consider the case of quasi-perpendicularity. The difference is significant because particles can cross back upstream for quasi-perpendicular shocks. There were analytical (Wu 1984; Krauss-Varban et al. 1989b) and hybrid simulation studies (Krauss-Varban et al. 1989a) of SDA in a nearly perpendicular bow shock for energetic electrons. Recently, Matsukiyo et al. (2011) performed 1D PIC simulation for the electron SDA in low Mach number quasi-perpendicular shocks in galaxy clusters.

In this paper, we present the results of 2D PIC simulations for quasi-perpendicular low M /high β_p shocks in solar flares. The upstream magnetic field makes angles of $\theta_B = 80^\circ, 82^\circ$, and 83.5° respectively to the shock normal and the shocks satisfy the subluminal condition, $V_{sh}/\cos\theta_B < c$, where V_{sh} is the shock speed in the upstream rest frame and c is the speed of light. In such a subluminal shock, electrons can then be reflected at the shock front due to the magnetic mirror effect and gain energy (e.g., Ball & Melrose 2001; Mann et al. 2006, 2009; Warmuth et al. 2009).

One difficulty in performing PIC simulations for SDA in solar flares is that they require sufficiently high energy electrons above the threshold energy for SDA in the simulation to obtain statistically reliable results. The commonly used Maxwellian distribution has too few above the threshold electrons to be used in a simulation. Herein we use a kappa distribution with $\kappa = 10$ for both injected ions and electrons. This increases the number of high energy electrons but does not significantly alter the original shock structure, which is determined by the bulk of the thermal particles. Although the kappa distribution is used for computational convenience in this paper, the kappa distribution may be physically a relevant distribution in the outflow driven electron-ion

jet (e.g., Yoon et al. 2006; Kašparová & Karlický 2009; Mann et al. 2006, 2009; Warmuth et al. 2009).

The goals of this paper are two-fold: (1) studying the formation and structure of such shocks, including the turbulent dissipation mechanism for collisionless shock sustenance and entropy creation, and (2) studying the particle acceleration mechanism relevant for the soft/hard X-ray flux observations in solar flares. We observe the same modified-two-stream instability (Krall & Liewer 1971) in the shock transition region as in the perpendicular shocks (Park et al. 2012) that can provide the turbulent dissipation in the downstream. Furthermore, a temperature anisotropy after the shock transition region is found to drive the electron whistler instability (e.g., Gary 1993).

As shown below, more SDA-accelerated electrons are found in the present simulations of the quasi-perpendicular case compared to the previously simulations of the perpendicular case (Park et al. 2012). In this context, we also extend the theoretical analysis in Mann et al. (2006, 2009); Warmuth et al. (2009) to include the electric potential jump at the shock front (e.g., Ball & Melrose 2001) and generalize the electron energy spectrum. Both our theoretical analysis and our simulations show a transition energy, $E_{\text{trans,p}}$, between the thermal and non-thermal photon spectrum that is determined by the minimum angle of θ_B . We find that the transition energy $E_{\text{trans,p}}$ and the spectral index δ from theory and our simulation are consistent with some of the X-ray spectra of solar flares from RHESSI (e.g., Altyntsev et al. 2012) in the energy range of $E \lesssim 40 \sim 100$ keV. Beyond this range, to maintain the power-law distribution up to $E \sim \text{MeV}$, additional mechanisms beyond the shock acceleration studied are required.

The rest of the paper is organized as follows. The simulation setup is described in Section 2. The shock structure and particle acceleration are described in Section 3. We summarize in Section 4.

2. SIMULATION SETUP

We use the fully-relativistic full PIC code OSIRIS (Fonseca et al. 2002) to study the formation of and particle energization in low- M , high- β_p shocks, where M is the Mach number and β_p is the ratio of thermal to magnetic pressure. To launch a shock, we use the moving wall boundary condition (Langdon et al. 1988; Park et al. 2012) at the right boundary of the 2D simulation box. The moving wall method generates a slowly propagating shock compared to the more standard fixed reflection boundary method, and allows for smaller box sizes and more efficient use of simulation time.

We adopt parameters typical of those found in solar flare reconnection outflows (Tsuneta 1996; Workman et al. 2011) as the upstream conditions for our shock. In particular, we use a plasma density $n = 5 \times 10^9/\text{cm}^3$, electron and ion temperatures $T_e = T_i = 0.8\text{keV}$ ($= 9.27 \times 10^6\text{K}$), and the magnetic field strength $B = 6\text{G}$ with $\beta_p \equiv 8\pi n(T_e + T_i)/B^2 = 8.93$. The magnetic field is in the x - y plane ($\mathbf{B} = B_x\hat{x} + B_y\hat{y}$) and has an angle of $\theta_B = 80^\circ$, 82° , and 83.5° from the shock normal (x -axis) in each simulation. We also performed another simulation where the upstream magnetic field is directed out of the simulation plane ($B = B_x\hat{x} + B_z\hat{z}$) and has an angle of $\theta_B = 80^\circ$ to compare the electron energy

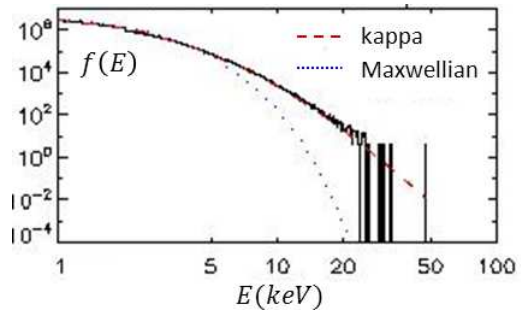


FIG. 1.— The initial energy distribution in the upstream rest frame from the simulation. The dashed line is a kappa distribution with $\kappa = 10$ and $T = 0.8\text{keV}$. The dotted line is a Maxwellian distribution with $T = 0.8\text{keV}$.

spectrum with that in the “in-plane” B -field simulation. A reduced ion/electron mass ratio of $m_i/m_e = 30$ is used to reduce computational demands. The Alfvén Mach number is chosen to be $M_A \equiv V_1\sqrt{4\pi m_i n}/B = 6.62$, which equates to an upstream plasma flow velocity in the shock rest frame, $V_1 = 0.032c$, for $m_i/m_e = 30$. If the real mass ratio, $m_i/m_e = 1836$, is used for the same M_A , then the upstream flow velocity would be 1226km/s ($= 0.0041c$). Effects of a realistic mass ratio are further discussed in Section 3.3. The super-fast-magnetosonic Mach number M satisfies $M \equiv M_A/\sqrt{1 + (5/6)\beta_p} = 2.28$. The ratio of the electron cyclotron frequency to the electron plasma frequency is $\Omega_{ce}/\omega_{pe} = 0.0265$. With these upstream values of M_A and β_p , the Rankine-Hugoniot relation (Tidman & Krall 1971) for the shocks with the angles used gives a compression ratio in the range of (2.06, 2.50), where the lower and the upper limits are calculated for 2D and 3D, respectively.

The simulation box is initialized with a kappa-distributed ion-electron plasma drifting with $V_d = 0.0213c$ and $T_e = T_i = 0.8\text{keV}$, where V_d is set to a smaller value than the upstream speed V_1 ($= 0.032c$) in the shock rest frame anticipating that the shock will be traveling to the left. In the upstream rest frame, the energy distribution is a kappa distribution such as

$$f(E) = \frac{2^{5/2}}{\sqrt{\pi}} \frac{1}{(2\kappa - 3)^{3/2}} \frac{\Gamma(\kappa + 1)}{\Gamma(\kappa - 1/2)} \frac{E^{1/2}}{T^{3/2}} \times \left(1 + \frac{2}{2\kappa - 3} \frac{E}{T}\right)^{-\kappa - 1}, \quad (1)$$

where Γ is the gamma function and $f(E)$ is normalized to 1, $\int_0^\infty dE f(E) = 1$. The kappa distribution approaches the Maxwellian distribution as κ goes to ∞ . Figure 1 shows the initial energy distribution in the upstream rest frame from the simulation. The dashed line is a kappa distribution in Equation (1) with $\kappa = 10$ and $T = 0.8\text{keV}$ and the dotted line is a Maxwellian distribution with the same temperature. The bulk parts ($E < 5\text{keV}$) of the two distributions are very similar. The implementation of the kappa distribution in OSIRIS is described in Appendix A.

A uniform external E_z field is set up along the z -axis with $E_z = -V_d B_y/c$. A new plasma of the same kappa distribution is constantly injected from the left boundary ($x = 0$) throughout the simulation. The simulation box

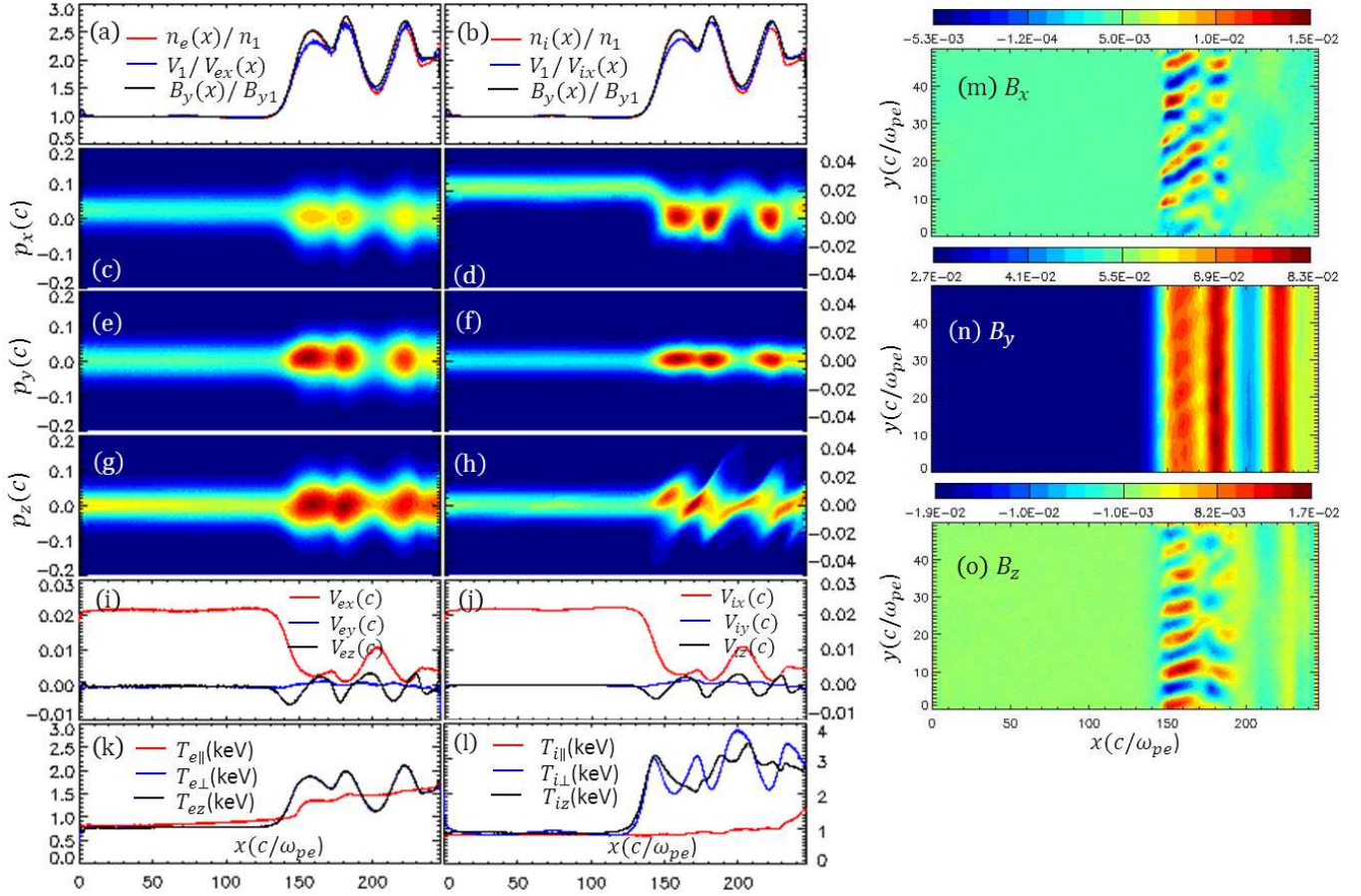


FIG. 2.— The ratios, n/n_1 , V_1/V_x , and B_y/B_{y1} , momentum distribution of $p_x - x$, $p_y - x$, and $p_z - x$, y -averaged flow velocity of V_x , V_y , and V_z , and temperature T_{\parallel} , T_{\perp} , T_z for the electrons (left column) and the ions (right column) at $t = 11200/\omega_{pe}$. (a) \sim (b) are calculated in the shock-rest frame and the other plots are obtained in the simulation frame. (m-o) show the B_x , B_y , and B_z fields in the $x - y$ space.

sizes are $L_x \times L_y = 250c/\omega_{pe} \times 50c/\omega_{pe}$. The grid size used is $dx = dy = 0.08c/\omega_{pe}$ and the time step used is $dt = 0.056/\omega_{pe}$. For each particle species, 196 particles per cell are used. The particle number/cell is fairly large to reduce numerical collisions and maintain the kappa distribution for a sufficiently long time.

A linear current deposition scheme is used for all simulations in this paper. A periodic boundary condition is used in the y -direction for both particles and fields. For fields, an open boundary condition is used in the x -direction. Particles that reach $x = 0$ are re-injected into the box with the initial kappa distribution. At $x = L_x$, a moving wall boundary condition is adopted (Park et al. 2012) and the moving wall speed is set to $V_{\text{wall}} = 0.004c$.

3. RESULTS AND ANALYSIS

3.1. Shock structure

In this subsection, we present results for the shock structure for $\theta_B = 80^\circ$ in-plane case only but other simulations for $\theta_B = 82^\circ$ and 83.5° also show similar shock structures. The electron energization via SDA shows different energy spectra for the different angles of θ_B as will be seen in the next subsection.

In Figure 2(a&b), we plot for both species the upstream to downstream ratios of density $n(x)/n_1$, flow speeds $V_1/V(x)$, and y -magnetic field, $B_y(x)/B_{y1}$. In

Figure 2(c-l), we plot the phase-space distributions of $p_x - x$, $p_y - x$, and $p_z - x$, the y -averaged flow velocity profiles of $V_x(x)$, $V_y(x)$, and $V_z(x)$, and the temperature profiles of $T_{\parallel}(x)$, $T_{\perp}(x)$, and $T_z(x)$ (where \perp and \parallel are perpendicular and parallel to the magnetic field $\mathbf{B}(x) \equiv B_x(x)\hat{x} + B_y(x)\hat{y}$, respectively), for the electrons (the left column) and the ions (the right column) at $t = 11200/\omega_{pe}$ for the $\theta_B = 80^\circ$ case.

In Figure 2, the shock front is at $x \approx 140c/\omega_{pe}$ and moves to the left with a speed of $0.01c$ in the simulation frame. In Figure 2(a&b), the compression ratio is $r = 2.5$ near the shock front and oscillates around 2.0 downstream, in reasonable agreement with the Rankine-Hugoniot relation (Tidman & Krall 1971). Figure 2(c-h) show that the electrons and ions are heated downstream but the ions are conspicuously less heated in the y -direction [Figure 2f]. In Figure 2(i&j), the flow velocity, $V_x = 0.021c$, in the upstream decreases downstream to the moving wall speed, $V_{\text{wall}} = 0.004c$. The z -component of the velocity, V_z , is oscillating around zero downstream due to the $\mathbf{E}_x \times \mathbf{B}_y$ -drift while $V_y \approx 0$. Figure 2(k&l) show that the downstream temperature is anisotropic, that is $T_{\perp} > T_{\parallel}$ with $T_{e\perp} = T_{ez} \approx 1.66\text{keV}$ and $T_{e\parallel} \approx 1.5\text{keV}$ for the electrons, and $T_{i\perp} = T_{iz} \approx 2.5\text{keV}$ and $T_{i\parallel} \approx 1.0\text{keV}$ for the ions.

Figure 2(m-o) show \mathbf{B} in the $x - y$ space. The B_x and

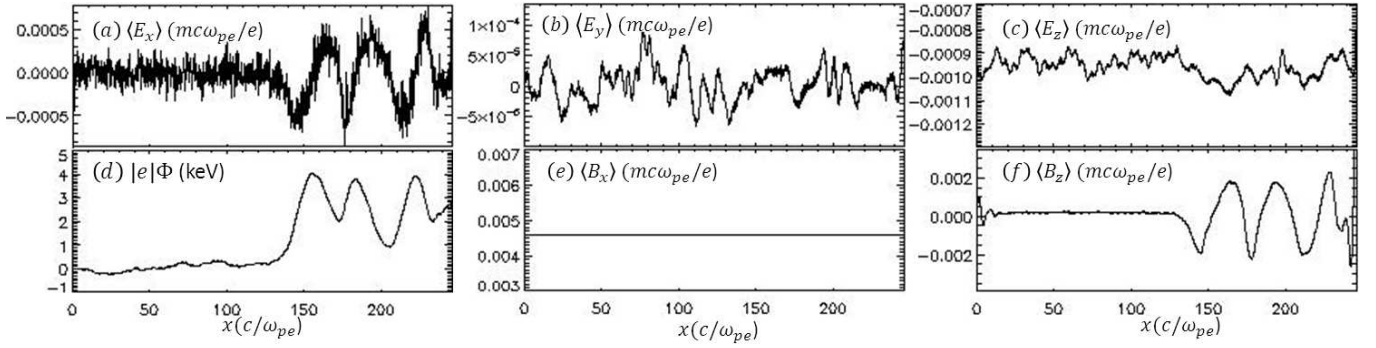


FIG. 3.— y -averaged \mathbf{E} and \mathbf{B} fields, and the potential energy $|e|\phi(x)$ at $t = 11200/\omega_{pe}$ measured in the shock rest frame.

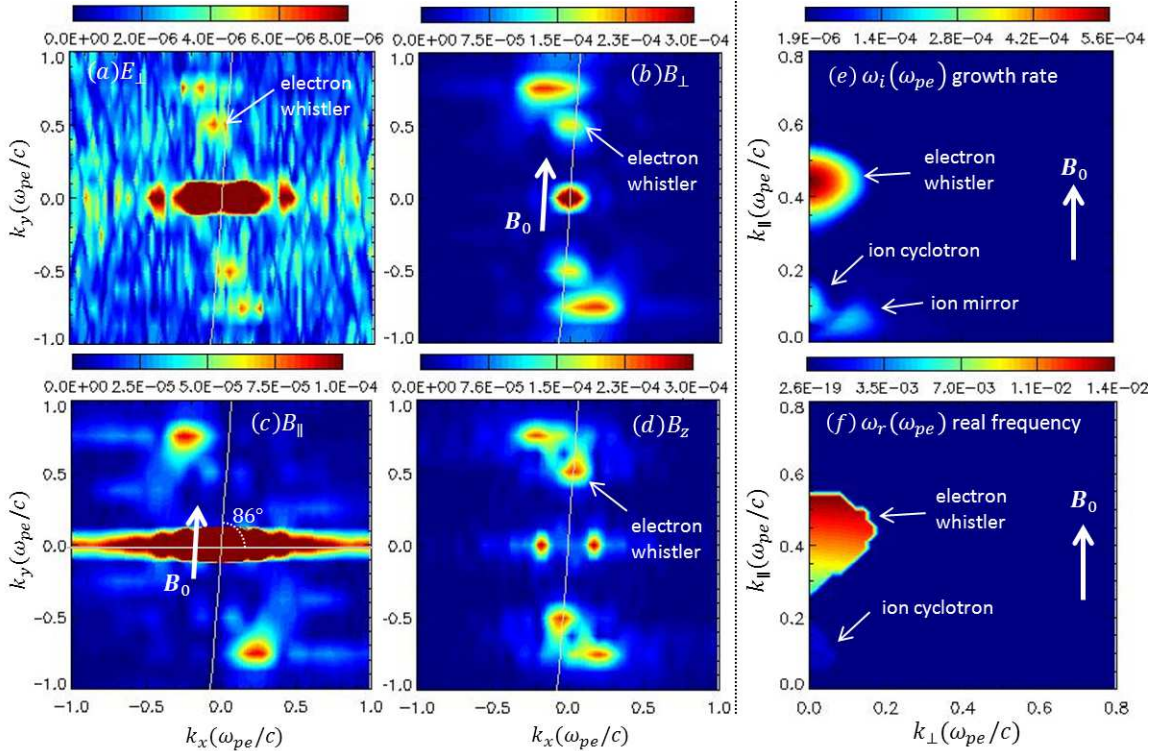


FIG. 4.— (a)–(d): Fourier spectra of the \mathbf{E} and \mathbf{B} fields in the $k_x - k_y$ space from the simulation. (e): Numerically solved growth rates of temperature anisotropy-driven instabilities in the region, $140 < x < 170(c/\omega_{pe})$ of Figure 2.

B_z fields show oscillatory patterns along the y -axis near the shock front ($x \sim 150c/\omega_{pe}$) and the B_y field shows a rippled surface along the y -axis. These variations are due to electron temperature anisotropy-driven instabilities, $T_{e\perp} > T_{e\parallel}$.

Figure 3 shows the y -averaged \mathbf{E} , \mathbf{B} , and the potential energy $|e|\Phi(x) = e \int_{x_1}^x E_x dx$ at $t = 11200/\omega_{pe}$, measured in the shock rest frame. The E_y , E_z , and B_x fields are approximately constant across the shock while E_x and B_z oscillate with a wave number $k = 0.2\omega_{pe}/c$ downstream. The potential energy jump $|e|\Delta\Phi$ at the shock front is $\sim 3.5\text{keV}$ [Figure 3d]. Some ions in the low energy tail reflect at the shock front and can drive the modified two-stream instability.

In Figure 4(a-d), we plot the Fourier spectra of the E_{\perp} , B_{\perp} , B_{\parallel} , and B_z fields, where \perp and \parallel are perpendicular and parallel to \mathbf{B}_0 , respectively. The $\mathbf{B}_0 (= B_{0x}\hat{x} + B_{0y}\hat{y})$

is an averaged field over $140 < x < 170(c/\omega_{pe})$ in Figure 2 and has an angle 86° from the x -axis. Two distinct dominant modes are excited by temperature anisotropy-driven instabilities ($T_{\perp} > T_{\parallel}$), one is along the \mathbf{B}_0 axis with $k = 0.5\omega_{pe}/c$ and another is slightly deviated from the \mathbf{B}_0 axis with $k = 0.8\omega_{pe}/c$. In Figure 4(d), the strong signals at $k_x = \pm 0.2\omega_{pe}/c$ are due to the oscillatory pattern of the B_z field along the x -axis as seen in Figure 3(f).

To analyze the spectra from the simulation, we numerically solve the dispersion relation (e.g., Gary 1993) in Figure 4(e&f). Here we assume bi-Maxwellian electron and ion distributions and a uniform background magnetic field B_0 . We use the parameters extracted from the simulation with $B_0 = 13.5\text{G}$, $T_{e\parallel} = 1.25\text{keV}$ and $T_{e\perp} = 1.66\text{keV}$ for the electrons, and $T_{i\parallel} = 0.86\text{keV}$ and $T_{i\perp} = 2.55\text{keV}$ for the ions, where \parallel and \perp are parallel

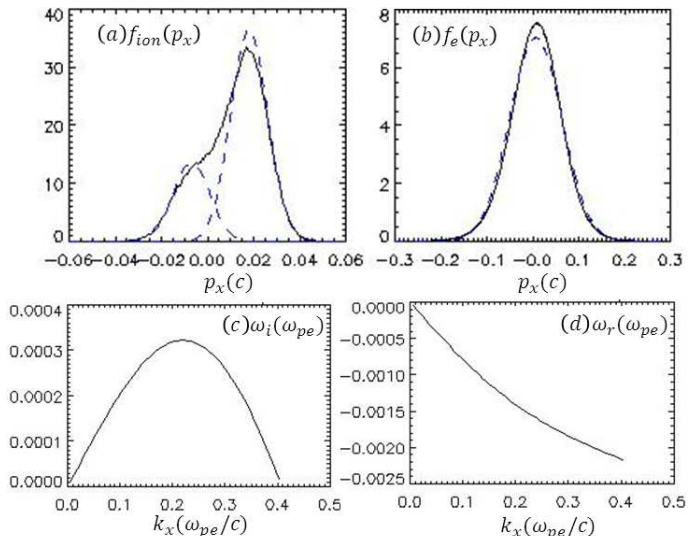


FIG. 5.— (a&b): Ion and electron distributions in the shock transition region, $135 < x < 155(c/\omega_{pe})$ at $t = 11200/\omega_{pe}$. We fit the distributions with Maxwellian distributions (dashed lines). (c&d): The growth rates and real frequencies obtained from the MTSI dispersion relation (Appendix B).

and perpendicular directions to B_0 , respectively.

In Figure 4(e), the electron whistler modes are centered on the B_0 axis with $k = 0.45\omega_{pe}/c$, the ion cyclotron modes centered on the B_0 axis with $k = 0.1\omega_{pe}/c$, and the ion mirror modes are obliquely off the B_0 axis with $k = 0.12\omega_{pe}/c$. The maximum growth rates are $\omega_i = 5.6 \times 10^{-4}\omega_{pe}$, $2.5 \times 10^{-4}\omega_{pe}$, and $2.0 \times 10^{-4}\omega_{pe}$ for the electron whistler, the ion cyclotron, and the ion mirror modes, respectively. In Figure 4(f), the real frequencies for the electron whistler and the ion cyclotron modes are around $\omega_r = 0.012\omega_{pe}$ and $0.0012\omega_{pe}$, respectively, and the ion mirror modes have zero real frequency. These are consistent with the analytical results (e.g., Gary 1993), $\Omega_{ci} < \omega_r < |\Omega_{ce}|$ for the electron whistler modes and $0 < \omega_r < \Omega_{ci}$ for the ion cyclotron modes.

The linear theory based on bi-Maxwellian distributions with the parameters found in the PIC simulations show that electron mirror modes are marginally stable (e.g., Gary & Karimabadi 2006). The oblique modes found in Figure 4(a~d) could be due to some unknown modes. However, given the fact that the actual distribution is not exactly a bi-Maxwellian (e.g., with flows) and the uncertainty in the temperature anisotropy measurements in the simulation, the oblique modes with $k = 0.8\omega_{pe}/c$ seen in the simulation [Figure 4(a~d)] may possibly still be a electron mirror-type of modes for a non-bi-Maxwellian distribution. In addition, the ion cyclotron/mirror modes are not observed in this simulation because of the small box size $L_y = 50c/\omega_{pe}$ and/or their relatively weaker growth.

Figure 5(a&b) shows the electron and ion distributions in the shock transition region in $135 < x < 155(c/\omega_{pe})$ at $t = 11200/\omega_{pe}$ from the simulation. We observe that 27% of the incoming ions are reflected at the shock front [Figure 5a] and the modified two-stream instability (MTSI) (e.g., Matsukiyo & Scholer 2003, 2006; Umeda et al. 2010, 2012) can be excited. Here we solve the MTSI in the electrostatic limit with its wave vector

along the x -axis (Appendix B). The electrons have a temperature of $T_{ex} = 1.65\text{keV}$ and drift with $V_{ex} = 0.0064c$ in the simulation frame [Figure 5b]. We fit the distributions using drifting Maxwellians. The electrons are magnetized with $B = 10G$ while the ions are assumed to be non-magnetized. In the electron rest frame, the drift velocities for the incoming and reflecting ions are $V_{xin} = 0.0116c$ and $V_{xre} = -0.0134c$, respectively. Both incoming and reflecting ions have a temperature of $T_{xin} = T_{xre} = 0.98\text{keV}$. In Figure 5(c&d), we solve the kinetic dispersion relation for the MTSI. The maximum growth rate is $\omega_i = 3.2 \times 10^{-4}\omega_{pe}$ at $k = 0.2c/\omega_{pe}$ and the real frequency is $\omega_r = -0.0015\omega_{pe}$.

Turbulent dissipation is needed to randomize the upstream flow to form collisionless shocks (e.g., Wu 1982). The macroscopic jump conditions across a shock are essentially independent of the source of microphysical turbulence, as long as there is such a source. Plasma instabilities in the shock transition region are natural sources for this needed turbulent dissipation and we consider three possible instabilities: (1) lower hybrid instability (the excited modes are in the $\mathbf{B} \times \nabla\mathbf{B}$ direction) (e.g., Zhou et al. 1983), (2) whistler instability, and (3) MTSI (e.g., Papadopoulos et al. 1971; Wagner et al. 1971). The lower hybrid instability is precluded in these 2D in-plane simulations where the \mathbf{B} -field is in the $x-y$ simulation plane. In addition, we notice that the shock structure (i.e. the compression ratio) in the simulation with an in-plane B field is the same as that with the out-of-plane B field which then precludes the whistler instability. We are led to conclude that the MTSI is the most likely candidate to provide the needed turbulence (e.g., Park et al. 2012).

3.2. particle heating via shock drift acceleration

In Figure 6, we plot the electron and ion energy distributions, $f(E) (= dN/dE)$ upstream [$50 < x < 155c/\omega_{pe}$ (b & e)] and downstream [$155 < x < 250c/\omega_{pe}$ (c & f)] at $t = 8400/\omega_{pe}$ for $\theta_B = 80^\circ$. We fit the thermal (bulk) part of the distributions using a kappa distribution with $\kappa = 10$ (dashed lines), yielding $T_e = T_i = 0.8\text{keV}$ upstream and $T_e = 1.58\text{keV}$ and $T_i = 1.8\text{keV}$ downstream. In Figure 6(a&d), we plot the electron and ion phase-space distributions in $E-x$, overlaid with B_y field to indicate the location of the shock front. Abundant non-thermal electrons are seen ahead of the shock at $x = 155c/\omega_{pe}$, traveling as far back as $x = 10c/\omega_{pe}$ [Figure 6a].

In Figure 6(b), the electron energy spectrum shows a deviation from a thermal distribution at $E \sim 12\text{keV}$ and the spectrum becomes steeper at $E \sim 50\text{keV}$. The dotted line in Figure 6(b) is the theoretical energy distribution via SDA when the electric potential energy jump $|e|\Delta\Phi \approx 3.5(\text{keV})$ at the shock front is considered (See Section 3.2.1). In Figure 6(e), the ion energy spectrum shows a deviation from a thermal distribution at $E \sim 15\text{keV}$ and the spectrum becomes steeper at $E \sim 30\text{keV}$.

In Figure 7(a-d), we plot a typical track of an electron experiencing SDA, overlaid with the shock front and the subsequent compression peaks [Figure 7a]. The electron is reflected at the shock front [Figure 7a] and gains energy from 8keV to 50keV [Figure 7c]. After the reflection, the electron drifts along the upstream magnetic field lines

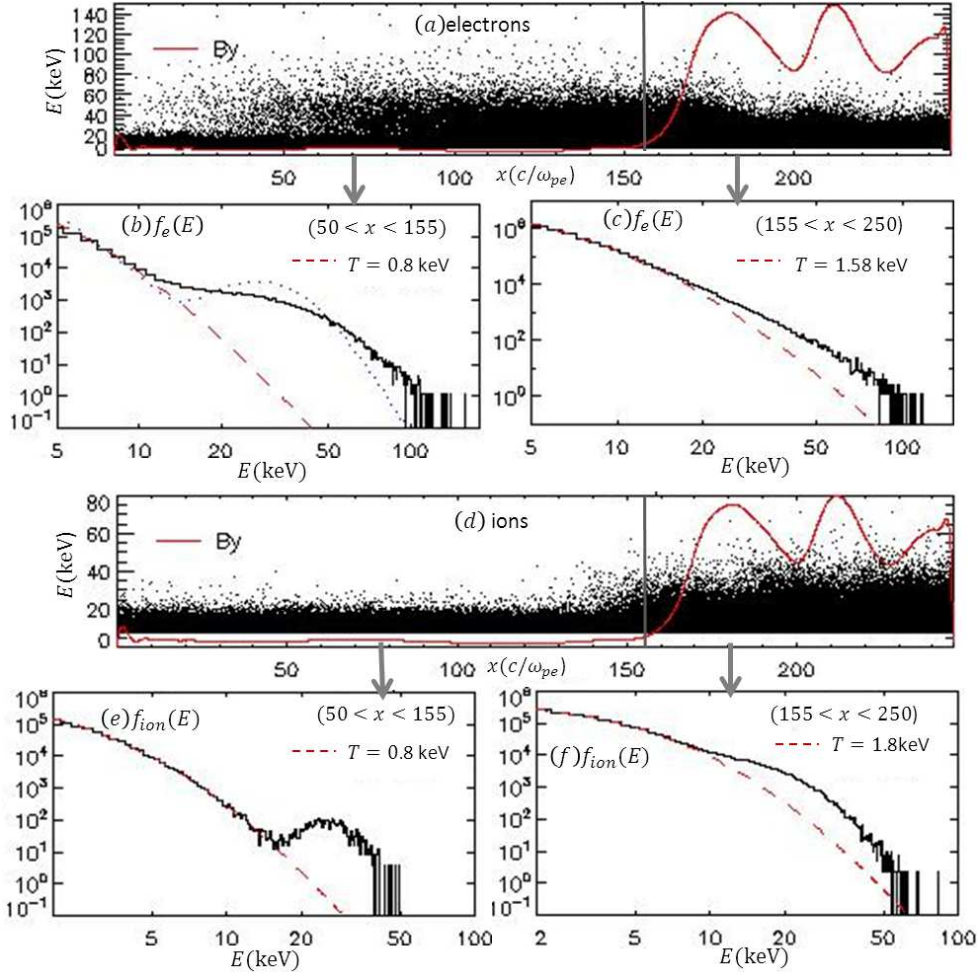


FIG. 6.— (a&d): Energy distribution vs. x -ranges where the B_y field is over-plotted with an arbitrary scale. The electron (b&c) and ion (e&f) energy distributions in upstream ($50 < x < 155c/\omega_{pe}$) and downstream ($155 < x < 250c/\omega_{pe}$) at $t = 8400/\omega_{pe}$. In (b), the dotted line is a theoretical energy distribution when the potential energy at the shock front is $e\Phi = -3.5$ (keV). We fit the thermal distributions with kappa distributions with $\kappa = 10$ (dashed lines).

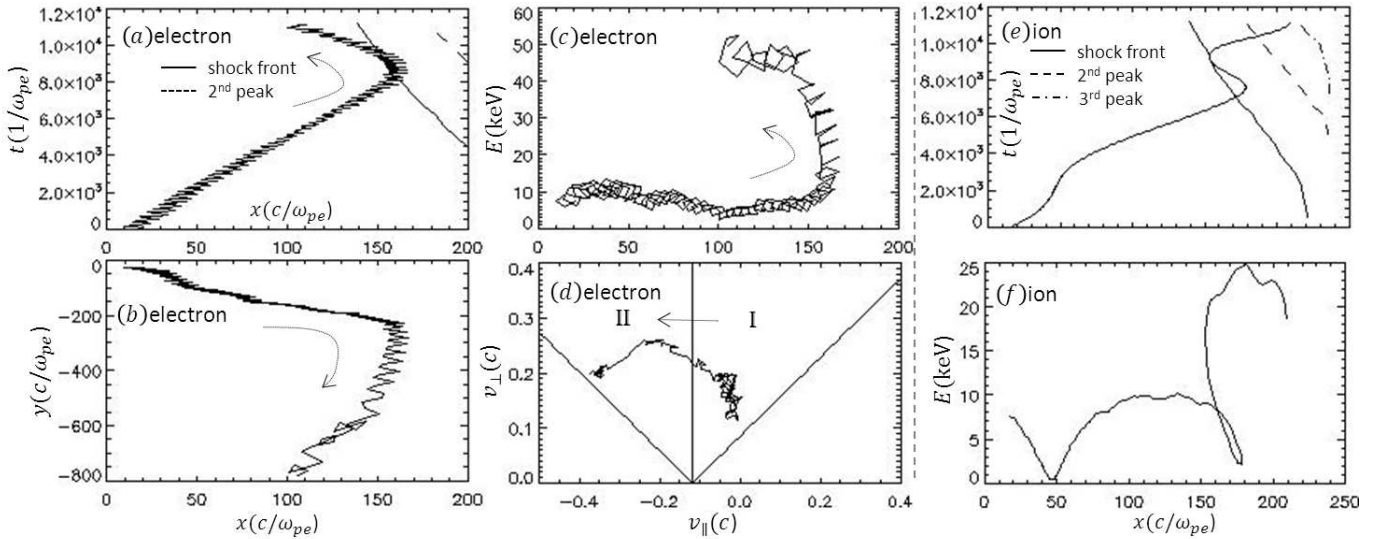


FIG. 7.— (a-d): A typical electron tracking experiencing SDA. (e&f): A typical ion tracking experiencing SDA.

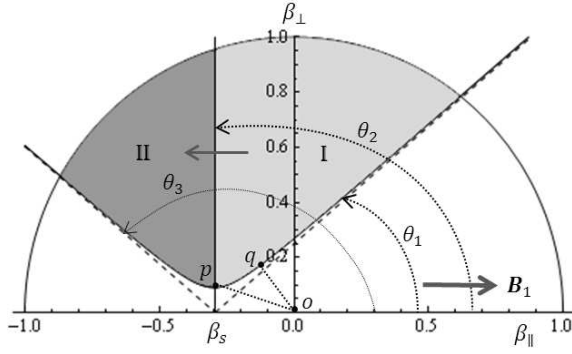


FIG. 8.— The condition for SDA in the $\beta_{\perp} - \beta_{\parallel}$ space of the upstream rest frame when $\beta_s (= V_{sh}/c \cos \theta_B) = -0.293$. The incoming electrons in the region I (light shaded) are transferred to the region II (dark shaded) after reflection (Mann et al. 2006, 2009). The hyperbolic curve is given by the potential energy $e\Phi = -3.5$ keV at the shock front, which approaches the straight dotted lines when $e\Phi \rightarrow 0$.

[Figure 7b]. In Figure 7(d), we plot the electron in the $v_{\perp} - v_{\parallel}$ phase-space. The electrons in the region I are transferred to the region II after the reflection.

In Figure 7(e&f), we plot a typical track for an ion experiencing SDA. Whether or not an ion gains energy via SDA depends on its incident speed and angle of incidence at the shock front (Kirk 1994). When the ion meets the shock front, it turns back toward the upstream with a larger gyro-radius [Figure 7a] and is accelerated by the E_z field. The kinetic energy of the ion increases from 5 keV up to 20 keV [Figure 7b]. A detailed analysis for ions experiencing SDA in perpendicular shocks was described in our previous work (Park et al. 2012).

3.2.1. Electron spectrum via SDA

In this subsection, we generalize the electron energy spectrum via SDA by Mann et al. (2006, 2009); Warmuth et al. (2009) to include the electric potential energy, $e\Phi$, at the shock front (e.g., Ball & Melrose 2001) and compare with the PIC simulation results.

First, we consider the de Hoffmann-Teller (dHT) frame (denoted by $'$) where the motional $E_z (= -V_1/cB_y)$ field vanishes. The dHT frame is obtained by boosting with $v_s = V_{sh}/\cos \theta_B$ along the magnetic field line in the upstream rest frame. (Here we consider the negative shock speed, $V_{sh} < 0$, for a shock traveling to the $-\hat{x}$ direction.) The maximum θ_B for the existence of the dHT frame is given by $\theta_{B\max} = \cos^{-1}(V_{sh}/c) (< 90^\circ)$.

In the dHT frame, the condition for an electron to reflect at the shock front is (e.g., Ball & Melrose 2001; Mann et al. 2006, 2009)

$$\beta'_{\perp} > \beta'_{\parallel} \tan \alpha_0 \text{ and } \beta'_{\parallel} > 0, \quad (2)$$

where \perp and \parallel are perpendicular and parallel to the upstream \mathbf{B}_1 , respectively, $\beta'_{\parallel,\perp} = v'_{\parallel,\perp}/c$, and $\alpha_0 = \sin^{-1} \sqrt{B_1/B_2} (\approx \sin^{-1} \sqrt{1/r})$. If we include the potential energy $e\Phi (< 0)$ at the shock front, the reflection condition, Equation (2), can be written in the non-relativistic limit by (e.g., Ball & Melrose 2001)

$$\beta'_{\perp} > \sqrt{\left(\beta'^2_{\parallel} - \frac{2e\Phi}{m_e c^2}\right)} \tan \alpha_0, \quad \beta'_{\parallel} > 0. \quad (3)$$

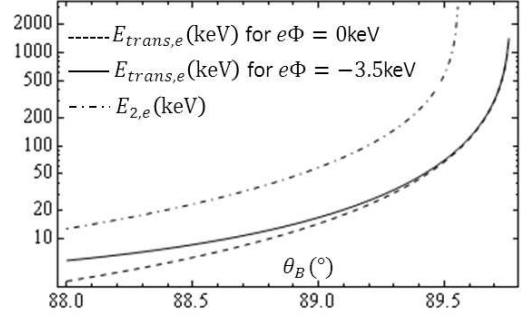


FIG. 9.— The transition energy $E_{trans,e}$ vs θ_B for $e\Phi = -3.5$ keV (solid) and 0 keV (dashed) from Eq.(8). The energy point $E_{2,e}$ vs θ_B (dot-dashed) from Eq.(9). Here $V_{sh} = 0.0041c$, $r = 2.5$ and $m_i/m_e = 1836$ ($M_A = 6.62$ and $\beta_p = 8.93$).

For relativistic electrons with $\beta'_{\parallel} \gg \sqrt{2|e\Phi|/m_e c^2} (= 0.117)$, the potential energy $e\Phi$ is negligible and Equation (3) is reduced to Equation (2).

Using the Lorentz transformation between the dHT frame($'$) and the upstream rest frame,

$$\beta'_{\parallel} = \frac{\beta_{\parallel} - \beta_s}{1 - \beta_{\parallel} \beta_s}, \quad \beta'_{\perp} = \frac{\beta_{\perp}}{\gamma_s (1 - v_{\parallel} \beta_s)}, \quad (4)$$

where $\beta_s = v_s/c (= V_{sh}/c \cos \theta_B)$ and $\gamma_s = 1/\sqrt{1 - \beta_s^2}$, Equation (3) is transformed in the upstream rest frame into

$$\beta_{\perp} > \gamma_s \tan \alpha_0 \left[(\beta_{\parallel} - \beta_s)^2 - \frac{2e\Phi}{m_e c^2} (1 - \beta_s \beta_{\parallel})^2 \right]^{1/2}, \quad \beta_{\parallel} > \beta_s. \quad (5)$$

The velocity of the electron after reflection in the dHT frame is given by $\beta'_{r\parallel} = -\beta'_{i\parallel}$ and $\beta'_{r\perp} = \beta'_{i\perp}$, where the indices i and r represent the incoming and reflected electron, respectively. In the upstream rest frame, one gets (Mann et al. 2006, 2009)

$$\beta_{i\parallel} = \frac{2\beta_s - \beta_{r\parallel}(1 + \beta_s^2)}{1 - 2\beta_{r\parallel}\beta_s + \beta_s^2}, \quad \beta_{i\perp} = \frac{\beta_{r\perp}}{\gamma_s^2 (1 - 2\beta_{r\parallel}\beta_s + \beta_s^2)}. \quad (6)$$

In Figure 8, we plot the SDA condition in the $\beta_{\perp} - \beta_{\parallel}$ space for $\beta_s = -0.293$ as an example (e.g., Mann et al. 2006, 2009). Equation (5) defines the region I (light shaded region) and the hyperbolic curve is given by the potential energy $e\Phi = -3.5$ keV at the shock front. When $e\Phi$ goes to zero, the hyperbolic curve approaches the straight dotted lines as seen in Mann et al. (2006, 2009). Equation (6) implies that the incoming electrons in the region I are transferred to the region II (dark shaded region) after reflection. As θ_B increases to $\theta_{B\max} (= \cos^{-1}(V_{sh}/c))$, β_s goes to -1 in Figure 8 and the number of electrons satisfying the reflection condition in Equation (5) decrease to zero. Therefore, no electron reflects at the shock front in the superluminal shocks (where $|\beta_s| \geq 1$) or the perpendicular shocks.

The threshold energy E_{thres} for SDA is given by the shortest distance from the origin to the hyperbolic curve,

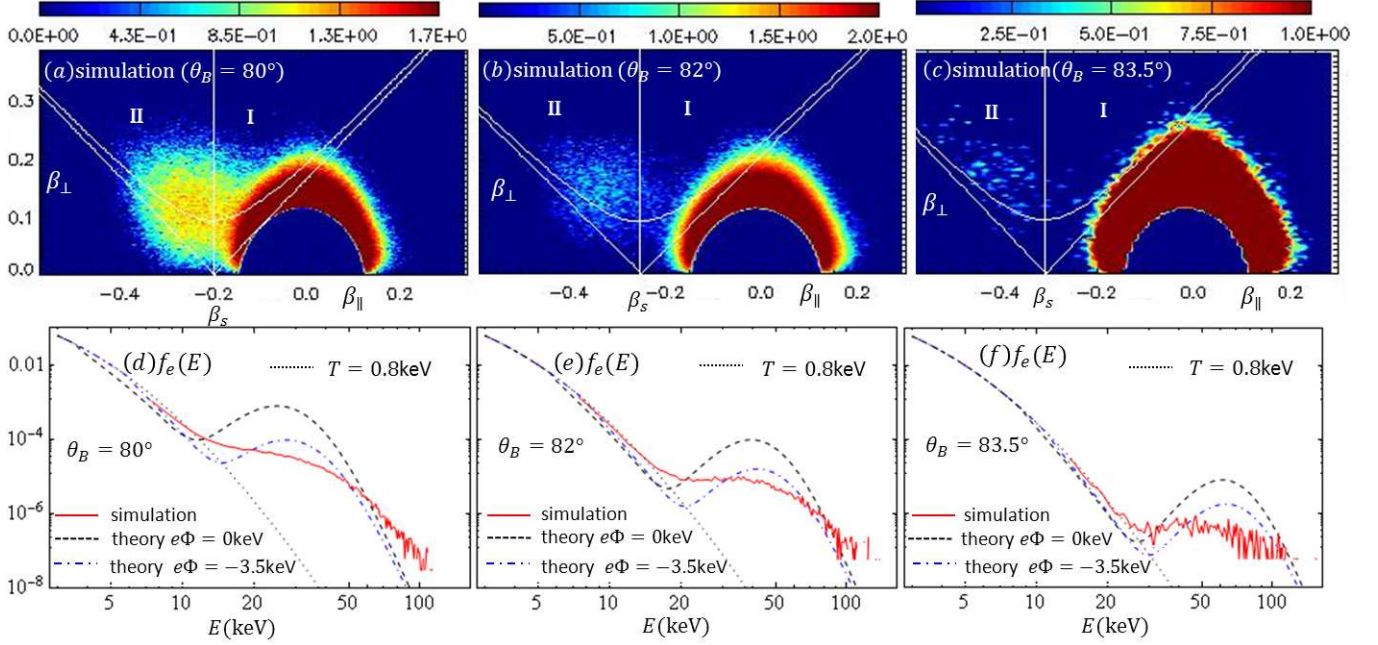


FIG. 10.— (a-c): Simulation results of the upstream electron distribution in the $\beta_{\perp}-\beta_{\parallel}$ space of the upstream rest frame for $\theta_B = 80^\circ, 82^\circ,$ and 83.5° . (d-f): The normalized upstream electron energy distributions in the upstream rest frame from the simulation (solid), and the theory with $e\Phi = 0$ (dashed) and $e\Phi = -3.5\text{keV}$ (dot-dashed) at the shock front. We fit the thermal distribution with a kappa distribution with $T = 0.8\text{keV}$ and $\kappa = 10$ (dotted). Here $V_{sh} = -0.032c$, $r = 2.5$ and $m_i/m_e = 30$ ($M_A = 6.62$ and $\beta_p = 8.93$).

$\overline{pq} (= \beta_{\text{thres}})$ in Figure 8, namely

$$E_{\text{thres}} = \left(1/\sqrt{1 - \beta_{\text{thres}}^2} - 1\right) m_e c^2, \quad \text{where} \quad (7)$$

$$\beta_{\text{thres}} = \sqrt{\frac{D^2 [(1 - \beta_s)^2 D^2 P^2 \{P - (1 + \beta_s^2)\} + \beta_s^2 - P]}{1 + D^2 (1 - P \beta_s^2)}},$$

where $D = \gamma_s \tan \alpha_0$ and $P = 2e\Phi/m_e c^2$.

The transition energy $E_{\text{trans},e}$ between thermal and non-thermal electron populations is given by the distance from the origin to the point p , $\overline{op} (= \beta_{\text{trans}})$, in Figure 8 such as

$$E_{\text{trans},e} = \left(1/\sqrt{1 - \beta_{\text{trans}}^2} - 1\right) m_e c^2, \quad \text{where} \quad (8)$$

$$\beta_{\text{trans}} = \beta_s^2 - (1 - \beta_s^2)(2e\Phi/m_e c^2) \tan^2 \alpha_0.$$

The energy point $E_{2,e}$ where the maximum energy ratio of the reflected to the incoming electron occurs is given by Ball & Melrose (2001) in the non-relativistic approximation, namely

$$E_{2,e} \approx \left(1/\sqrt{1 - \beta_2^2} - 1\right) m_e c^2,$$

$$\beta_2 = 2\beta_s \cos(\alpha_0/2), \quad (9)$$

Beyond $E = E_{2,e}$, the spectral index δ , defined as in $f(E) \propto E^{-\delta}$, increases. Figure 9 shows how the transition energy $E_{\text{trans},e}$ for $e\Phi = -3.5\text{keV}$ (solid) and 0keV (dashed), and $E_{2,e}$ (dot-dashed) varies with θ_B when $V_{sh} = 0.0041c$, $r = 2.5$ and $m_i/m_e = 1836$ ($M_A = 6.62$ and $\beta_p = 8.93$).

The reflected electron distribution in the upstream rest

frame is written as

$$f_r(\beta_r) = f_i[\beta_i(\beta_r)](d^3\beta_i/d^3\beta_r)\Theta(\beta_s - \beta_{r\parallel}) \times \Theta\left(\beta_{r\perp} - \gamma_s \tan \alpha_0 \left[(\beta_s - \beta_{r\parallel})^2 - \frac{2e\Phi}{m_e c^2}(1 - \beta_s \beta_{r\parallel})^2\right]^{1/2}\right), \quad (10)$$

where Θ is the step function and the term $d^3\beta_i/d^3\beta_r$ is given by the Jacobian determinant,

$$\frac{d^3\beta_i}{d^3\beta_r} = \frac{\beta_{i\perp}}{\beta_{r\perp}} \left| \frac{\partial(\beta_{i\perp}, \beta_{i\parallel})}{\partial(\beta_{r\perp}, \beta_{r\parallel})} \right| = \frac{(1 - \beta_s)^4}{(1 - 2\beta_{r\parallel}\beta_s + \beta_s^2)^4}. \quad (11)$$

Here we let the incoming distribution in Equation (10) be a semi-relativistic kappa distribution (Mann et al. 2006, 2009),

$$f_i(\beta_i) = c_\kappa \left(1 + \frac{2(\gamma_i - 1) m_e c^2}{2\kappa - 3 T}\right)^{-\kappa - 1}, \quad (12)$$

where $\gamma_i = 1/\sqrt{1 - \beta_i^2}$ and $c_\kappa = 1/\int d^3\beta_i f_i(\beta_i)$.

We calculate the upstream electron energy distributions, $f(E) = f(\beta)d\beta/dE$, in the upstream rest frame using Equations (6-12) to obtain

$$f(\beta) = \begin{cases} 2\pi\beta^2 \int_{-1}^1 dt f_i(\beta) & \text{for } \beta < \beta_{\text{thres}} \\ 2\pi\beta^2 \left(\int_{-1}^{t_3} dt + \int_{t_1}^1 dt \right) f_i(\beta) & \text{for } \beta_{\text{thres}} \leq \beta < \beta_{\text{trans}}, \\ 2\pi\beta^2 \int_{t_3}^{t_2} dt \frac{d^3\beta_i}{d^3\beta_r} f_i[\beta_i(\beta, t)] & \\ + 2\pi\beta^2 \left(\int_{-1}^{t_2} dt + \int_{t_1}^1 dt \right) f_i(\beta) & \\ \dots & \text{for } \beta \geq \beta_{\text{trans}} \end{cases} \quad (13)$$

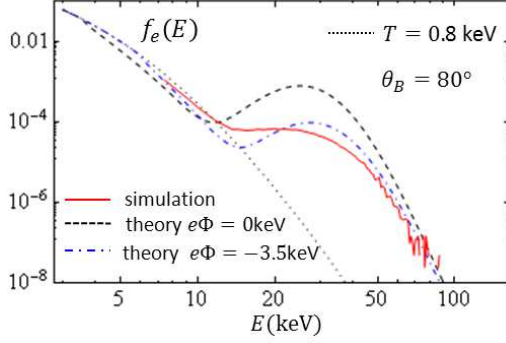


FIG. 11.— The normalized upstream electron energy distribution in the upstream rest frame from the out-of-plane upstream B -field simulation (solid) ($\mathbf{B}_1 = B_{1x}\hat{x} + B_{1z}\hat{z}$). The dashed and dot-dashed lines are theoretical results for $e\Phi = 0$ and $e\Phi = -3.5\text{keV}$ at the shock front, respectively.

where $t = \cos\theta$ and θ is the electron's pitch angle, i.e., the angle between β and \mathbf{B}_1 . The boundaries $t_1 (= \cos\theta_1)$, $t_2 (= \cos\theta_2)$, and $t_3 (= \cos\theta_3)$ as shown in Figure 8 are given as $t_2 = \beta_s/\beta$, and roots of the equation,

$$t_{1,3}^2 \{1 + D^2(1 - P\beta_s^2)\} - 2t_{1,3}D^2\frac{\beta_s}{\beta}(1 - P) + \frac{D^2}{\beta^2}(\beta_s^2 - P) - 1 = 0. \quad (14)$$

In Figure 10(a-c), we plot the upstream electron distribution in the $\beta_\perp - \beta_\parallel$ space of the upstream rest frame from the simulations for $\theta_B = 80, 82$ and 83.5° . Electrons in region I are transferred to region II. As θ_B increases, the number of electrons participating in SDA decreases since the energy threshold for SDA in Equation (7) increases.

In Figure 10(d-f), we plot the normalized upstream electron energy distributions, $f(E) (= 1/NdN/dE)$, in the upstream rest frame for $\theta_B = 80, 82$ and 83.5° . We compare the results of Equation (13) for $e\Phi = 0$ (dashed) and -3.5keV (dot-dashed) with the simulation result (solid). The dotted line is the incoming kappa distribution with $T = 0.8\text{keV}$ and $\kappa = 10$. Using Equation (8), the transition energy points are given by $E_{\text{trans},e} = 11.3\text{keV}, 16.5\text{keV},$ and 24.2keV for the angles, $\theta_B = 80^\circ, 82^\circ,$ and 83.5° , respectively, when $e\Phi = -3.5\text{keV}$. Using Equation (9), the energy points $E_{2,e}$'s, beyond which the spectral index increases, are given by $E_{2,e} = 34\text{keV}, 56\text{keV},$ and 93keV for the angles, $\theta_B = 80^\circ, 82^\circ,$ and 83.5° , respectively. Here $V_{sh} = -0.032c$, $r = 2.5$ and $m_i/m_e = 30$ ($M_A = 6.62$ and $\beta_p = 8.93$).

In Figure 11, we plot the upstream electron energy distribution in the upstream rest frame from the out-of-plane upstream B -field simulation (solid) where $\mathbf{B}_1 = B_{1x}\hat{x} + B_{1z}\hat{z}$ and $\theta_B = 80^\circ$. The dashed and dot-dashed lines are the theoretical results for $e\Phi = 0$ and $e\Phi = -3.5\text{keV}$ at the shock front, respectively. In this simulation, the temperature anisotropy-driven instabilities seen in Figure 4 are precluded. By direct comparison with the electron energy distribution in Figure 10(d), the simulation result in Figure 11 is closer to the theoretical result for $e\Phi = -3.5\text{keV}$. That is, the high energy tail is steeper in Figure 11. This implies that the tempera-

ture anisotropy-driven instabilities near the shock front can contribute to further electron acceleration, possibly via the interaction between electrons and perturbed magnetic fields. There is a still discrepancy between the theory with $e\Phi = -3.5\text{keV}$ and the simulation around the transition energy, $E_{\text{trans},e} = 11.3\text{keV}$. This is probably due to the effects of small-scale waves generated in the transition region as indicated by Matsukiyo et al. (2011).

3.2.2. Bremsstrahlung radiation

Electrons accelerated via SDA move along the magnetic field lines as can be seen from the electron tracking in Figure 7(b) and will collide with ions to emit bremsstrahlung radiation. In the low-frequency limit of $\omega b/\gamma v \ll 1$, where ω is a photon angular frequency, b is the impact parameter, v is the electron speed, and $\gamma = 1/\sqrt{1 - (v/c)^2}$, the number of photons per unit frequency per unit volume per unit time produced by the bremsstrahlung process is (e.g., Rybicki & Lightman 1979)

$$\frac{dN}{d\omega dV dt} = \frac{16Z^2 e^6 n_e n_i}{3c^3 m_e^2 \hbar^2 \omega} \int_{v_{\min}}^c \frac{\gamma}{v} \ln\left(\frac{\gamma m_e v^2}{\hbar \omega}\right) f(v) dv, \quad (15)$$

where $f(v)$ is a normalized electron distribution and v_{\min} is determined by the equation $\hbar\omega = (\gamma_{\min} - 1)mc^2$.

Given the electron distributions in Figure 10(d-f), we calculate the number of photons per unit time(sec) per unit energy(keV) using Equation (15) for the ion density of $n_i = n_e$ and the volume of the region emitting the X-rays, $V = 10^{27}\text{cm}^3$. In Figure 12(a&b), we show the photon distribution for $\theta_B = 80$ (solid), 82 (dashed), and 83.5 (dot-dashed) when the electron distribution is given by the theoretical distribution in Equation (13) with $e\Phi = -3.5\text{keV}$ [Figure 12a] and by the simulation [Figure 12b]. The dotted line is the photon distribution when the electron distribution is given by a kappa distribution with $T = 0.8\text{keV}$ and $\kappa = 10$. Here $V_{sh} = -0.032c$, $r = 2.5$ and $m_i/m_e = 30$ ($M_A = 6.62$ and $\beta_p = 8.93$).

In Figure 12(c), we plot the averaged photon distribution of $80^\circ \leq \theta_B \leq \theta_{B\text{max}} (= 88.17^\circ)$ from the theoretical distribution in Equation (13) with $e\Phi = 0$ (dashed) and $e\Phi = -3.5\text{keV}$ (solid). In Figure 12(d), we plot the averaged photon distribution of $\theta_B = 80, 82,$ and 83.5° from the electron distribution given by Equation (13) with $e\Phi = 0$ (dashed) and $e\Phi = -3.5\text{keV}$ (dot-dashed), and from the simulations (solid). In Figure 12(d), we notice that the theoretical result with $e\Phi = -3.5\text{keV}$ (dot-dashed) is in good agreement with the simulation result (solid).

In Figure 12(d), the simulation result shows that the transition energy between the thermal and non-thermal photon spectrum is $E_{\text{trans},p} \approx 10\text{keV}$ and the energy point beyond which the photon spectrum becomes steeper, is $E_{2,p} \approx 40\text{keV}$. The spectral index is $\delta = 3$ (simulation) and $\delta = 2.2$ (theory with $e\Phi = -3.5\text{keV}$) in $10\text{keV} < E < 40\text{keV}$ and $\delta = 7$ (simulation) in $E > 40\text{keV}$. For emission from multiple shocks with different θ_B 's, the transition energy $E_{\text{trans},p}$ and $E_{2,p}$ would be dominated by the shock with the minimum θ_B . Note that the transition energy $E_{\text{trans},p}$ for the photon distribution is a bit smaller than $E_{\text{trans},e}$ for the elec-

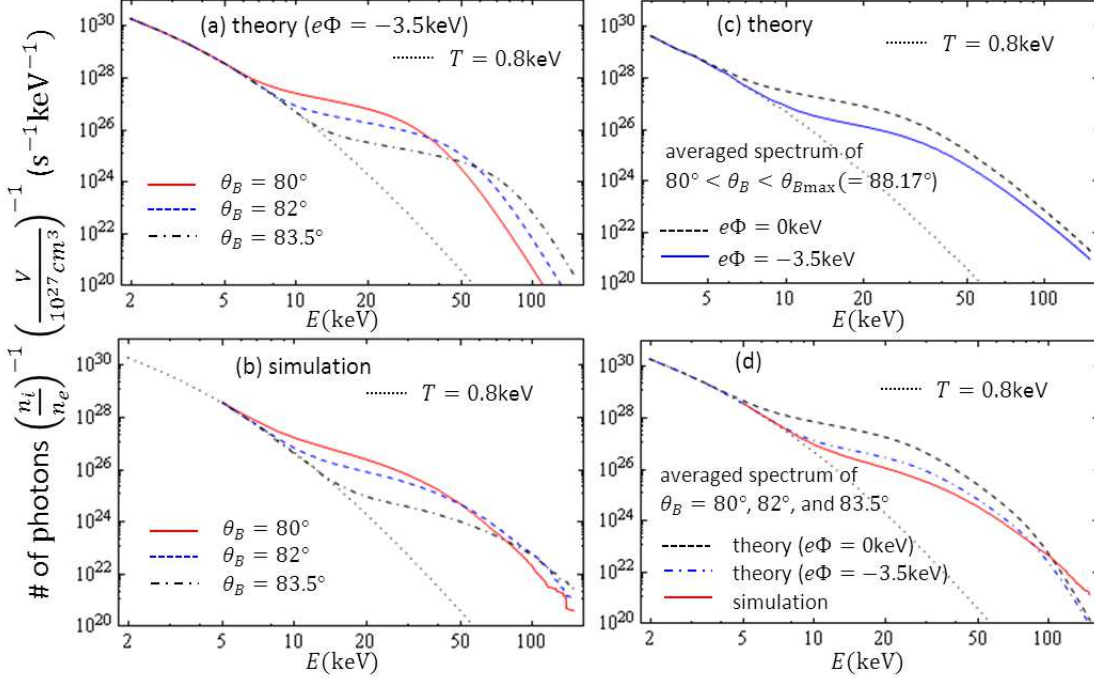


FIG. 12.— (a&b): The photon distribution via bremsstrahlung radiation for $\theta_B = 80^\circ$, 82° , and 83.5° when the electron distributions are given by Eq.(13) and by simulations. (c): The averaged photon distribution of $80^\circ \leq \theta_B \leq \theta_{B\max}(= 88.17^\circ)$ from the theoretical distributions with $e\Phi = 0$ and -3.5keV . (d): The averaged photon distribution of $\theta_B = 80^\circ$, 82° , and 83.5° . The dotted line is the photon distribution when the electron distribution is a kappa distribution with $T = 0.8\text{keV}$ and $\kappa = 10$. Here $V_{sh} = -0.032c$, $r = 2.5$ and $m_i/m_e = 30$ ($M_A = 6.62$ and $\beta_p = 8.93$).

tron distribution because bremsstrahlung photons are produced by electrons with higher energies than the photon energy (e.g., Holman 2003). The energy point $E_{2,p}$ is approximately given by Equation (9).

RHESSI data for several solar flares (Table I in Altyntsev et al. (2012)), shows that the spectral index δ is in the range $2.5 < \delta < 3$ and the transition energy is in the range $12.1 \text{ keV} < E_{\text{trans},p} < 29.2 \text{ keV}$. Therefore, the electron energization via SDA well explains some of the RHESSI X-ray spectra for the energy regime, $E < E_{2,p}$ and how the transition energy is related with the shock geometry, i.e., the minimum θ_B .

The observed RHESSI spectra do not show a steepening beyond $E = E_{2,p}$, and thus the theory herein cannot by itself account for the electron acceleration to produce those photons. This indicates that additional mechanisms, such as diffusive shock acceleration, are required for further electron energization to maintain the power-law spectrum up to $E \sim \text{MeV}$. It is not unreasonable to expect that solar flares involve multiple acceleration mechanisms operating on a range of scales.

3.3. Effects of a realistic proton/electron mass ratio on the spectra

With the actual ion/electron mass ratio of $m_i/m_e = 1836$, the shock speed in the upstream rest frame is reduced by $\sqrt{30/1836}$ compared to our simulations when the Mach number M and the plasma β_p are fixed. The compression ratio r and the electric potential energy $e\Phi$ are unchanged for a fixed M and β_p (e.g., Hoshino 2001). Therefore, the shock structure are not expected to change for a realistic mass ratio simulation.

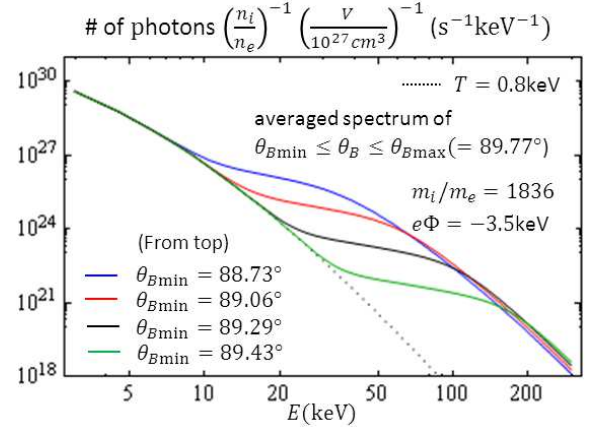


FIG. 13.— The averaged photon distribution of $\theta_{B\min} \leq \theta_B \leq \theta_{B\max}(= 89.77^\circ)$ from the theoretical distributions in Equation (13) with $e\Phi = -3.5\text{keV}$ for several minimum values of θ_B . Here $V_{sh} = 0.0041c$, $r = 2.5$ and $m_i/m_e = 1836$ ($M_A = 6.62$ and $\beta_p = 8.93$). The transition energy increases as $\theta_{B\min}$ increases.

The electron energy spectrum in Equation (6) depends only on β_s , α_0 , and $e\Phi$. For a fixed M and β_p , α_0 ($\equiv \sin^{-1} \sqrt{B_1/B_2}$) and $e\Phi$ are unchanged. From the definition of β_s ($\equiv V_{sh}/c \cos \theta_B$), we only need to change the angle from θ_B into θ'_B to obtain the electron energy spectrum for the mass ratio $m_i/m_e = 1836$ from that with $m_i/m_e = 30$,

$$\theta'_B = \cos^{-1} \left[\frac{\cos \theta_B}{\sqrt{1836/30}} \right]. \quad (16)$$

For example, the averaged spectrum with $80^\circ \leq \theta_B \leq \theta_{B\max}(= 88.17^\circ)$ for $m_i/m_e = 30$ corresponds to that with $88.73^\circ \leq \theta_B \leq 89.77^\circ$ for $m_i/m_e = 1836$.

In Figure 13, we plot the averaged photon distribution of $\theta_{B\min} \leq \theta_B \leq \theta_{B\max}(= 89.77^\circ)$ for a real ion/electron mass ratio, $m_i/m_e = 1836$, from the electron distribution given by Equation (13) with $e\Phi = -3.5\text{keV}$. Here $V_{sh} = 0.0041c$ and $r = 2.5$ ($M_A = 6.62$ and $\beta_p = 8.93$). The different values of $\theta_{B\min}$, from $\theta_{B\min} = 88.73^\circ$ to 89.43° , give the different transition energy points, from $E_{\text{trans},p} = 10$ to 35 keV. The power indices of the photon spectrum are nearly the same as $\delta \sim 2.2$ in $E_{\text{trans},p} < E < E_{2,p}$, where $E_{2,p}$ runs from 40 to 150 keV.

4. CONCLUSION

In summary, we studied quasi-perpendicular, low M /high β_p shocks with full PIC 2D simulations using a reduced ion/electron mass ratio $m_i/m_e = 30$. The shock compression ratio we found was in agreement with the Rankine-Hugoniot relation. Whistler instabilities driven by downstream temperature anisotropy were observed. A modified two-stream instability due to the incoming and reflecting ions in the shock transition region was also observed.

Abundant non-thermal electrons accelerated via SDA were observed upstream. We compared the electron energy distribution from the simulations with the distributions derived by extending a theoretical model (Mann et al. 2006, 2009; Warmuth et al. 2009) and found that they reasonably agree with each other.

In the perpendicular shocks, however, SDA can be achieved only by particles transmitting into the downstream, and their energy gains are smaller than those of the reflected ones in quasi-perpendicular shocks here

(e.g., Ball & Melrose 2001). Therefore, such abundant non-thermal electrons observed in this paper were not seen in the perpendicular shocks (e.g., Park et al. 2012).

We calculated the photon flux via bremsstrahlung radiation from the electron distributions from both the theory and the simulations. We showed that a transition energy, $E_{\text{trans},p}$, marking the transition from a thermal to a non-thermal part of the photon spectrum, is determined by the minimum θ_B from multiple shocks with different θ_B 's in $\theta_{B\min} \leq \theta_B \leq 90^\circ$. Different solar flares have different $\theta_{B\min}$'s in their termination shocks and therefore can show different transition energy points.

From the simulations, the averaged photon spectrum of $\theta_B = 80^\circ, 82^\circ, \text{ and } 83.5^\circ$ gives a spectral index $\delta \sim 3$ in $10\text{keV} < E < 40\text{keV}$ and the spectral index increases beyond $E = 40\text{keV}$. The spectral index $\delta \sim 3$ as well as the transition energy, $E_{\text{trans},p} = 10\text{keV}$, well explains some of the RHESSI X-ray spectra in the energy regime, $E < 40\text{keV}$. To account for the spectral index of the RHESSI X-ray spectrum up to $E \sim \text{MeV}$, however, additional mechanisms other than SDA are required.

Note that although our simulations were performed using $m_i/m_e = 30$, we analytically scaled the results to the realistic ion/electron mass ratio, and found that the predicted photon spectra are indeed insensitive to this mass ratio.

This work was supported by NSF under Grant PHY-0903797, by DOE under Grant No. DE-FG02-06ER54879 and Cooperative Agreement No. DE-FC52-08NA28302, and by NSFC under Grant No. 11129503. We also thank the OSIRIS consortium for the use of OSIRIS. The research used resources of NERSC.

APPENDIX

GENERATION OF A KAPPA DISTRIBUTION

To generate a kappa distribution, we use the random number distribution by Leitner et al. (2011). We denote $\{N_i(0, 1) | i = 1, 2, \dots, N\}$ as a set of normally distributed random numbers with the mean of 0 and the deviation of 1, and $\{U_i(0, 1) | i = 1, 2, \dots, N\}$ as a set of uniformly distributed random numbers between $[0, 1]$. Then a sequence of the random number x_i given by

$$x_i = b_1 N_i(0, 1) + b_2 U_i(0, 1) x_{i-1} \quad (\text{A1})$$

generates a 1D kappa distribution with the mean of 0 and the deviation of 1, and the coefficients, b_1 and b_2 determine the index κ (Figure 8 in Leitner et al. 2011).

To implement the kappa generator in OSIRIS, we determine the particle's initial momentum \mathbf{p} as

$$\mathbf{p}_i = \mathbf{p}_{th} x_i + \mathbf{p}_d, \quad (\text{A2})$$

where x_i is given by Equation (A1), \mathbf{p}_{th} and \mathbf{p}_d are the thermal and the drift momentum, respectively. For $\kappa = 10$, we choose $b_1 = 0.58$ and $b_2 = 1.15$. Then a sequence of \mathbf{p}_i in Equation (A2) generates a 3D kappa distribution in Figure 1.

DISPERSION RELATION FOR THE MODIFIED TWO-STREAM INSTABILITY

The kinetic dispersion relation for electrostatic instabilities is

$$1 + \sum_{s=e,i} K_s(\mathbf{k}, \omega) = 0, \quad (\text{B1})$$

where $K_s(\mathbf{k}, \omega)$ is the susceptibility. For magnetized electrons with isotropic Maxwellian distributions, $K_e(\mathbf{k}, \omega)$ is given by (Gary 1993)

$$K_e(\mathbf{k}, \omega) = \frac{\omega_{pe}^2}{v_{eth}^2 k^2} \left[1 + \xi_e^0 e^{-\lambda_e} \sum_{m=-\infty}^{\infty} I_m(\lambda_e) Z(\xi_e^m) \right], \quad (\text{B2})$$

where v_{eth} is the thermal velocity, I_m is the modified Bessel function of the first kind, $\lambda_e = k_{\perp}^2 v_{eth}^2 / \Omega_e^2$, $\Omega_e = eB / (m_e c) (< 0)$, Z is the plasma dispersion function, and $\xi_e^m = (\omega - m\Omega_e) / (\sqrt{2}k_{\parallel} v_{eth})$. For unmagnetized ions with drifting Maxwellian distributions,

$$K_i(\mathbf{k}, \omega) = -\frac{\omega_{pi}^2}{2v_{ith}^2 k^2} Z'(\xi_i), \quad (\text{B3})$$

where $\xi_i = (\omega - \mathbf{k} \cdot \mathbf{V}_{id}) / (\sqrt{2}k v_{ith})$ and $'$ is the derivative with respect to ξ_s .

Here we consider that $\mathbf{B} \approx B_y \hat{y}$, $\mathbf{k} = k_x \hat{x} + V_{sd} \hat{z}$. Then the term $\xi_e^0 Z(\xi_s^m)$ in Equation (B2) becomes $-\omega / (\omega - m\Omega_e)$ as k_{\parallel} goes to 0. The dispersion relation for the MTSI in the electrostatic limit becomes

$$1 + \frac{\omega_{pe}^2}{v_{eth}^2 k^2} \left(1 - e^{-\lambda_e} \sum_{m=-\infty}^{\infty} I_m(\lambda_e) \frac{\omega}{\omega - m\Omega_e} \right) - \sum_{s=in,re} \frac{\omega_{ps}^2}{2v_{sth}^2 k^2} Z'(\xi_s) = 0. \quad (\text{B4})$$

REFERENCES

- Altynsev, A. A., Fleishman, G. D., Lesovoi, S. V., & Meshalkina, N. S. 2012, *ApJ*, 758, 138
- Ball, L. & Melrose, D. B. 2001, *Publ. Astron. Soc. Aust.*, 18, 361
- Blackman, E. G. & Field, G. B. 1994, *PRL*, 73, 3097
- Fonseca, R. A., et al. 2002, *Lect. Notes Comput. Sci.*, 2331, 342
- Forbes, T.G. 1998, *Solar Physics*, 117, 97
- Gary, S. P. 1993, *Theory of Space Plasma Microinstabilities*, (Cambridge Univ. Press, Cambridge)
- Gary, S. P. & Karimabadi, H. 2006, *J. Geophys. Res.*, 111, A11224
- Guo, F. & Giacalone, J. 2010, *ApJ*, 715, 406
- Guo, F. & Giacalone, J. 2012, *ApJ*, 753, 28
- Hoshino, M. 2001, *Prog. Theo. Phys. Suppl.* 143, 149
- Holman, G. D., Sui, L., Schwartz, R. A., & Emslie, G. 2003, *ApJ*, 595, L97
- Kašparová, J. & Karlický, M. 2009, *A&A*, 497, L13
- Kirk, J. G. 1994, in *Plasma Astrophysics*, ed. Kirk, J. G., Melrose, D. B., & Priest, E. R. (Springer-Verlag, Berlin)
- Krall, N. A. & Liewer, P. C. 1971, *Phys. Rev. A*, 4, 5
- Krauss-Varban, D., Burgess, D., & Wu, C. S. 1989a, *J. Geophys. Res.*, 94, 15089
- Krauss-Varban, D. & Wu, C. S., J. 1989b, *Geophys. Res.*, 94, 15367
- Langdon, B., Arons, J., & Max, C. 1988, *PRL*, 61, 7
- Leitner, M., Leubner, M. P., & Vörös, Z. 2011, *Physica A*, 390, 124
- Lin R. P., Krucker, S., Hurford, G. J., et al. 2003, *ApJ*, 595, L69
- Mann, G., Aurass, H., & Warmuth, A. 2006, *A&A*, 454, 969
- Mann, G., Warmuth, A., & Aurass, H. 2009, *A&A*, 494, 669
- Matsukiyo, S., Scholer, M., 2003, *J. Geophys. Res.*, 108, A12
- Matsukiyo, S., Scholer, M., 2006, *J. Geophys. Res.*, 111, A06104
- Matsukiyo, S., Ohira, Y., Yamazaki, R., & Umeda, T., 2011, *ApJ*, 742, 47
- Papadopoulos, K., Wagner, C. E., & Haber, I. 1971, *PRL* 27, 982
- Park, J., Workman, J. C., Blackman, E. G., Ren, C., & Siller, R. 2012, *Phys. Plasmas*, 19, 062904
- Rybicki, G. B. & Lightman, A. P. 1979, *Radiative Processes in Astrophysics* (John Wiley & Sons, New York)
- Tidman, D. A. & Krall, N. A. 1971, *Shock Waves in Collisionless Plasmas* (Wiley-Interscience, New York)
- Tsuneta, S. 1996, *ApJ*, 456, 840
- Umeda, T., Kidani, Y., Yamao, M., Matsukiyo, S., and Yamazaki, R. 2010, *J. Geophys. Res.*, 115, A10250
- Umeda, T., Kidani, Y., Matsukiyo, S., and Yamazaki, R. 2012, *J. Geophys. Res.*, 117, A03206
- Wagner, E., Papadopoulos, K., & Haber, I. 1971, *Phys. Lett. A* 35, 440
- Warmuth, A., Mann, G., & Aurass, H. 2009, *A&A*, 494, 677
- Workman, J. C., Blackman, E. G., & Ren, C. 2011, *Phys. Plasmas*, 18, 092902
- Wu, C. S. 1982, *Space Science Rev.*, 32, 83
- Wu, C. S., Winske, D., Zhou, Y. M., et al. 1984, *Space Science Rev.*, 37, 63
- Wu, C. S. 1984, *J. Geophys. Res.*, 89, 8857
- Yoon, P. H., Rhee, T., & Ryu, J. 2006, *Geophys.*, 111, A09106
- Zhou, Y. M., Wong, H. K., Wu, C. S., & Winske, D. 1983, *J. Geophys. Res.*, 88, 3026